PHOTONICS Research

Continuous-wave single-mode quantum cascade laser at 5.1 THz based on graded sampled grating design

Weijiang Li,[1,2] Yu Ma,[1,2] Yunfei Xu,[1,2] Junqi Liu,[1,2,4] Lijun Wang,[1,2,5] Ning Zhuo,[1,6] Quanyong Lu,[3] Jinchuan Zhang,[1] Shenqiang Zhai,[1] Shuman Liu,[1,2] and Fengqi Liu[1,2,3]

[1]Key Laboratory of Semiconductor Materials Science, Institute of Semiconductors, Chinese Academy of Sciences, Beijing 100083, China
[2]College of Materials Science and Opto-Electronic Technology, University of Chinese Academy of Sciences, Beijing 101408, China
[3]Division of Quantum Materials and Devices, Beijing Academy of Quantum Information Sciences, Beijing 100193, China
[4]e-mail: jqliu@semi.ac.cn
[5]e-mail: ljwang@semi.ac.cn
[6]e-mail: zhuoning@semi.ac.cn

Received 16 June 2022; revised 29 September 2022; accepted 3 October 2022; posted 4 October 2022 (Doc. ID 467974); published 4 November 2022

We report on the terahertz (THz) quantum cascade lasers in continuous-wave (CW) operation with an emitting frequency above 5 THz. Excellent performance with a smaller leakage current and higher population inversion efficiency is obtained by one-well bridged bound-to-continuum hybrid quantum design at 5 THz. By designing and fabricating a graded metallic sampled distributed feedback grating in the waveguide, the first single-mode THz quantum cascade laser at 5.13 THz in CW operation mode is achieved. The maximum single-mode optical power of ~48 mW is achieved at 15 K with a side-mode suppression ratio above 24 dB. This will draw great interest in the spectroscopy applications above the 5 THz range for THz quantum cascade lasers. © 2022 Chinese Laser Press

https://doi.org/10.1364/PRJ.467974

1. INTRODUCTION

Terahertz (THz) frequency radiation (~0.1–10 THz) has attracted great attention from fundamental research to industrial applications owing to its great potential in the applications of biomedical diagnosis, astrophysics, security scanning and public safety, noninvasive inspections, and chemical remote sensing, etc. [1–5]. For many of these applications, compact and highly efficient THz sources are most needed. Since its first demonstration in 2002 [6], THz quantum cascade laser (QCL) [7] based on unipolar intersubband transitions has become a promising candidate. During the last two decades, the performance of THz QCL has been greatly improved, including high emitting powers (exceeding 2 W in pulsed mode [8] and 0.2 W in continuous-wave (CW) mode [9], respectively), a high operating temperature of ~250 K [10], and broad emitting spectra ranging from 1 to 5.6 THz [11,12]. THz waves with frequencies that exceed 5 THz are of great significance for applications such as high-resolution spectra of gas species and shallow donor transitions in isotope-enriched semiconductors [13,14]. However, the studies on GaAs-based QCLs with frequencies beyond 5 THz are limited due to the strong optical losses in the so-called reststrahlen band induced by the resonant optical phonon absorption (~36 meV in GaAs) [15–17]. Pronounced degradations of device performances (output power, operating temperature, threshold current density) were observed when the lasing band exceeds 5 THz [18,19]. Up to now, the highest lasing frequency of GaAs-based THz QCL reaches 5.6 THz, but it only operates in pulsed mode. The peak output power of the device is 178 mW at 10 K. The highest emitting frequency of a single-mode device is 4.98 THz with a peak output power of ~33.5 mW [12]. Up to now, CW mode, especially in single-mode operation for THz QCLs above 5 THz, has yet to be demonstrated for practical applications.

In this work, we report the first CW operation of THz QCLs at frequencies above 5 THz based on an optimized bound-to-continuum hybrid quantum design with suppressed current leakage channels. A peak output power of 220 mW in pulsed mode is achieved with Fabry–Perot (FP) devices. In CW mode, a maximum optical power of 79 mW and a spectral range of 4.92–5.26 THz are obtained at 15 K for an FP device. To achieve single-mode emission and also improve the power extraction efficiency for the lossy distributed feedback (DFB) waveguide, we present a graded sampled grating DFB design, the maximum single-mode power is enhanced by a factor of 2 compared with normal coated device, and up to 48 mW at

5.13 THz with a side-mode suppression ratio (SMSR) above 24 dB is obtained (at 15 K).

2. DESIGN AND FABRICATION

The active core is based on an optimized bound-to-continuum hybrid quantum design [20] composed of repeated periods of four quantum wells (QWs) based on the GaAs/$Al_{0.18}Ga_{0.82}As$ material system, with one QW serving as a bridge between a two-QWs active region and one-QW injector. This design could significantly suppress the current leakage channels by reducing the coupling between the lasing states and the parasitic states. The layer sequence in one module from the injector barrier is as follows (thickness in angstroms): **53.2**/93.5/**10.4**/105.6/**34.4**/87.5/**43.8**/(65.4 + 100.6), where $Al_{0.18}Ga_{0.82}As$ layers are in bold and the underlined layer is doped with Si to 7×10^{16} cm^{-3}. As shown in Fig. 1, electrons are injected from the state 1 into the upper laser level 5 of the next stage at the design bias (0.059 V/module), then transited diagonally from the level 5 to the miniband combined with lower laser levels 4 and 3, and subsequently transported through the bridge well and scattered very quickly into the injector ground state by LO phonon. The diagonal transitions ($f_{5,4} = 0.29$) help to secure a decent upper-state lifetime while the lower-state lifetime is significantly reduced, which further enhances the population inversion. The key parameters of the design are listed in Table 1. According to the expression for the tunneling injection between the injector state and the upper state [21], the current density is defined as

$$J = qN_s \frac{2|\Omega|^2 \tau_\perp}{1 + \Delta^2 \tau_\perp^2 + 4|\Omega|^2 \tau_u \tau_\perp}, \quad (1)$$

where q is the electronic charge, N_s is the sheet density, $2\hbar\Omega$ is the coupling energy between the injector state 1 and upper state 5, $\hbar\Delta$ is the energy detuning from resonance, $\tau_\perp$ is the in-plane electron momentum relaxation time, and τ_u is the upper state lifetime. Therefore, a thin injection barrier was designed to increase the value of Ω for a high injection efficiency in previous works [21,22]. However, the thinner barrier would lead to a larger carrier leakage from state 6 to states 7, 8 and a carrier leakage from ground state 1 to lower states 2, 3, 4. As a compromise, we use an injection barrier of 5.32 nm to decrease the leakage carriers from the ground injector state 1 to states 2, 3, 4 while maintaining the coupling with upper state 5, which can reduce leakage currents and allow more electrons to be injected into the upper state via resonant tunneling. In addition, one QW bridged between the active QWs and extraction QW is also employed to ensure a smaller threshold current density (J_{th}) since it can reduce the parasitic current through the smaller wave function coupling caused by the spatial separation of the transition level 6 and parasitic levels. Meanwhile, the bridge QW also reduces the overlap between the upper and lower states, which is beneficial to the lifetime of the upper state. According to the calculation parameters of the active region listed in Table 1, the normalized oscillation strength f for all the three possible leakages between the laser levels and the parasitic levels is reduced for our design. Thus, the leakage channels between the upper level 5' and parasitic level 7, the minibands 6 and parasitic levels 7 and 8, as the arrows denote in Fig. 1, are suppressed. This is beneficial to achieve a low threshold operation through the above optimization. It is apparent that the above design strategy would lead to a reduced leakage current density.

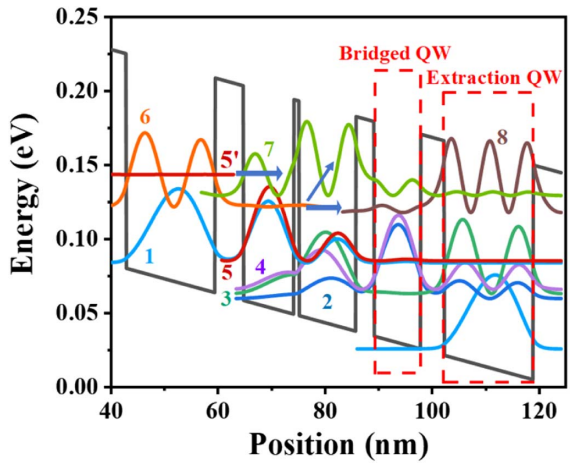

Fig. 1. Schematic conduction band diagram of one module of the four-quantum-wells active region under an applied electric field of 9.9 $kV \cdot cm^{-1}$.

For THz QCLs, metal-stripe buried grating is a simple and effective way to obtain precise frequency control and robust single-mode operation through an effective refractive index modulation by patterning the grating into the active region [23,24]. Furthermore, due to the small confinement factor (0.1–0.5) of the THz QCLs with semi-insulating surface-plasmon (SISP) waveguide [17], mode selection for edge-emitting devices is generally achieved by first-order DFB gratings. However, for the uniform grating designs, the optical field is accumulated in the center of the laser cavity because of the over-coupled feedback mechanism [25], and a sampled grating technology was adopted to enhance the output powers of THz DFB QCLs [24] and mid-infrared QCLs [26,27] by regulating the optical coupling strength. In order to improve the optical powers of the front facet while ensuring the single-mode performance and avoiding catastrophic failure of the high-reflectivity (HR) coating on the rear facet, we adopted a graded

Table 1. Key Computed Parameters of the Active Region at a Temperature of 100 K[a]

$\hbar\omega_{5,4}$	$\hbar\omega_{5,3}$	$z_{5,4}$	$z_{5,3}$	$f_{5,4}$	$f_{5,3}$	$f_{6,7}$	$f_{5',7}$	$f_{6,8}$	$\Omega_{1,5}$	τ_5
19.2 meV	22.1 meV	29.4 Å	17 Å	0.29	0.11	0.05	0.007	0.012	0.65 meV	1.45 ps

[a]$\hbar\omega$ is the photon energy, z the dipole matrix element, f the normalized oscillator strength ($f = 0.067 \times F$, F the oscillator strength), $\Omega_{1,5}$ the coupling energy between the injector ground state of the previous period and the upper state, and τ_5 the upper state lifetime.

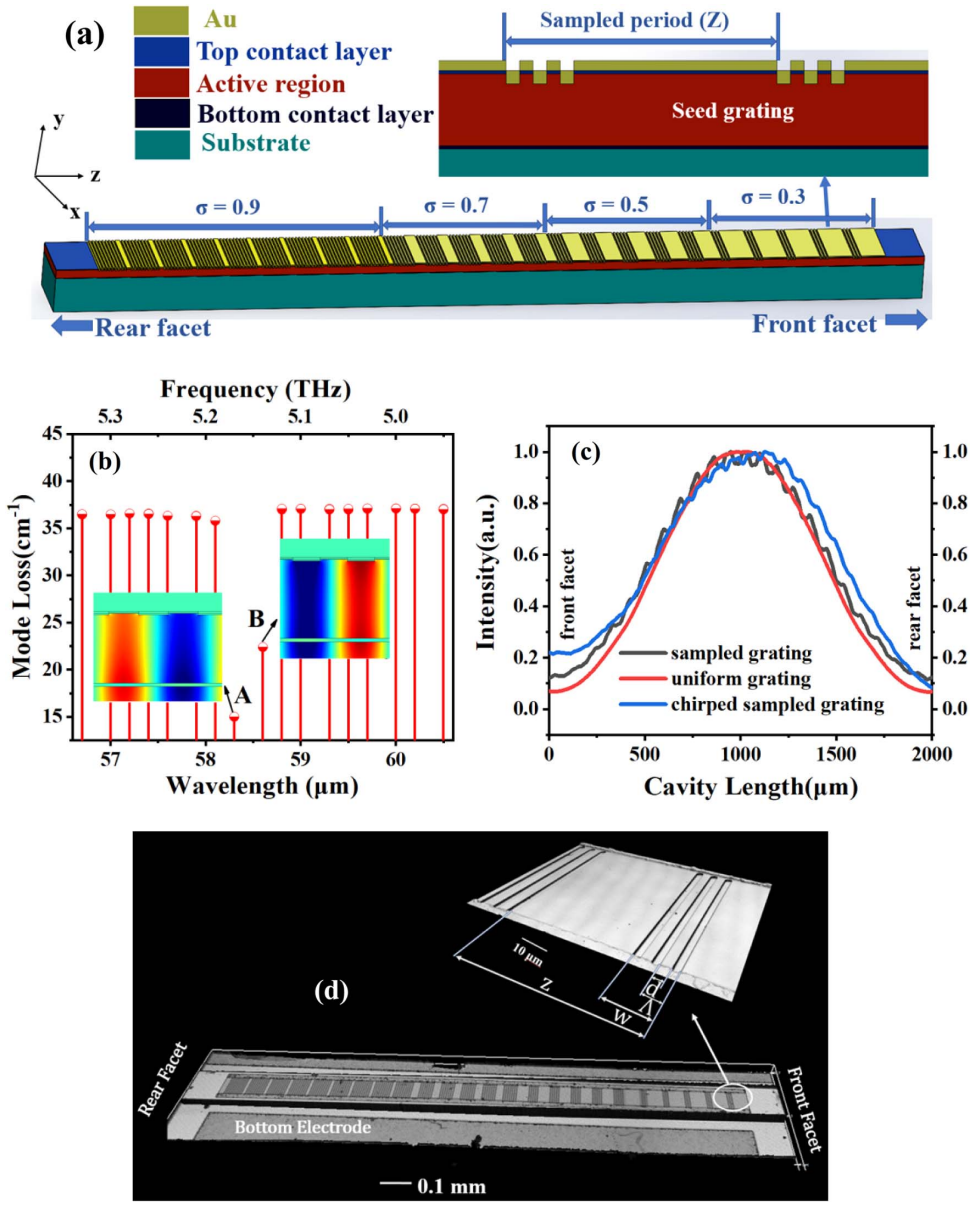

Fig. 2. (a) Schematic diagram of the graded sampled grating DFB QCL. (b) Calculated mode loss versus wavelength for the QCL with graded sampled grating. (c) The envelope distribution of mode intensities ($|E_y|^2$) inside lasers with three different grating structures. (d) The top view images of the DFB QCL structure and one-period sampled grating taken with a 3D stereomicroscope and one-period sampled grating.

sampled grating (SG) design to engineer light intensity distribution by controlling both the field distribution and coupling coefficient; thus, the longitudinal spatial hole-burning and the degeneration of the yield are overcome. The period of the sampled grating can be expressed as

$$2\Lambda = N\frac{\lambda_0}{n_{\text{eff}}}, \tag{2}$$

$$\frac{1}{2n_{\text{eff}}Z} = \frac{1}{\lambda_{\pm 1}} - \frac{1}{\lambda_0}, \tag{3}$$

where Λ is the period of the seed grating, N is the grating order, λ_0 is the Bragg wavelength, n_{eff} is the effective refractive index, $\lambda_{\pm 1}$ is the wavelength of ± 1st order supermodes, and Z is the period of the sampled grating. The schematic diagram of the graded sampled grating DFB QCL and images taken with a 3D stereomicroscope are presented in Figs. 2(a) and 2(d). Here, the seed grating period $\Lambda = 8.1\,\mu\text{m}$ with a duty cycle of $d/\Lambda = 0.6$ was selected, and we chose the sampled grating period of $Z = 77\,\mu\text{m}$ to obtain a reliable single-mode operation, while the sampling duty cycle ($\sigma = W/Z$) of the graded sampled grating gradually varies from 0.9 to 0.3 along the cavity. The front facet with a duty cycle of 0.3 can be regarded as a lower reflectivity mirror due to a lower coupling coefficient, while the rear facet with a duty cycle of 0.9 is equivalent to a mirror with higher reflectivity. With these parameters, we

simulated the mode distribution of uniform grating, sampled grating, and graded sampled grating via the two-dimensional finite element method. Figure 2(b) depicts the calculated mode loss for different modes of the graded sampled grating. A is the desired mode that has a lower mode loss. Normalized mode intensity distributions ($|E_y|^2$) along the laser cavity of the three grating configurations are shown in Fig. 2(c). Most of the optical field inside the uniform grating is localized in the center of the laser cavity due to its over-coupled mechanism. The output powers of the front and rear facets are enhanced by lowering the effective coupling coefficient of the sampled grating laser, while the graded sampled grating laser increases the output power of the front facet even further by decreasing the sampling duty cycle toward the front facet. For the graded sampled laser, the intensity of the light field at the front facet is approximately twice that of the rear facet.

3. EXPERIMENTAL DETAILS

The QCL structure was grown by molecular beam epitaxy on a semi-insulating GaAs substrate, with an 11 μm thick active region (180 cascade modules) sandwiched by an $n = 5\times10^{18}\,\mathrm{cm}^{-3}$ Si doped top contact layer (100 nm) and a 500 nm thick n-GaAs bottom contact layer Si-doped with a density of $n = 3\times10^{18}\ \mathrm{cm}^{-3}$. The wafers were processed into ridges with widths of 250 μm and 150 μm via conventional photolithography and wet chemical etching techniques. For the DFB QCLs, the graded sampled grating was etched on the top of the active region with an etching depth of 400 nm. Two Ge/Au/Ni/Au stripes were deposited on the highly doped upper layer to form ohmic contact, and the uncovered absorbing edge can suppress higher-order transverse modes. The Ti/Au layer was then evaporated on the top of the ridge and the bottom contact layer. Finally, the substrate was thinned to 120 μm to improve heat dissipation. The processed wafer was cleaved into devices with different cavity lengths with the front and rear facets uncoated, and the devices were indium soldered and wire-bonded on copper submounts.

For sample characterization, FP QCLs and DFB QCLs with graded sampled grating structures were fabricated, based on SISP waveguides. Copper submounts with lasers were mounted on a cold plate in a liquid-helium cryostat with 3 mm thick TPX (4-polyethylene-1) windows. The optical powers were collected by a thermopile detector (Ophir 3A-P-THz) calibrated by Thomas Keating absolute power meter and corrected for the TPX window transmittance of 78%. The emission spectra were measured using a Fourier-transform infrared spectrometer (Bruker, Vertex 80v).

4. RESULTS AND DISCUSSION

Figure 3(a) shows the typical light-current-voltage (L-I-V) characteristics for FP devices from front facets with various dimensions at 8 K. The devices operated in pulsed mode and rectangular pulses of 10 μs duration repeated at 1 kHz were used for biasing. Low threshold current densities (J_{th} are approximately between 0.11 and 0.13 $\mathrm{kA/cm^2}$) were observed in these devices, which are much lower than that in Refs. [12,18,19]. This is a direct consequence of reduced parasitic and leakage currents in our design, as discussed in the active region design section. According to Ref. [15], the parasitic current density (J_{par}) corresponds to a nonradiative electron transport process based on resonant tunneling and optical phonon emission. The I-V characteristics suggest that there is a J_{par} existing between the voltage point and the initial alignment point, as shown in Fig. 3(c). Thus, the experimental J_{par} of these devices are between 74 and 99 $\mathrm{A/cm^2}$, determined by I-V characteristics at the points where the differential resistance is locally maximal [15]. At 8 K, a peak output power of 220 mW was emitted by a device with a dimension of $0.25\times5\ \mathrm{mm}^2$. We extract the waveguide loss $\alpha_w = 11.1\ \mathrm{cm}^{-1}$ by comparing the acquired J_{th} between lasers with different cavity lengths. Note that such a high waveguide loss is directly related to the strong optical absorption near the reststrahlen band to the emitting frequencies. The temperature-dependent L-I-V characteristics of this device are shown in Fig. 3(b). A maximum operating temperature of 100 K is obtained. A representative spectrum at 8 K is also shown in the inset. Figure 3(c) depicts the CW L-I-V characteristics of the device with a ridge width of 150 μm and a cavity length of 2 mm at different heat sink temperatures, while Fig. 3(d) shows the lasing spectra from the device at different injection currents at 15 K. A maximum CW optical power of 79 mW at 15 K is achieved. The device exhibits multimode spectra and broadening toward high frequencies with increasing injection current, where the highest emitting frequency at high currents reaches up to 5.26 THz.

Figure 4 illustrates the performance for single-mode CW operation of the DFB QCL with graded sampled grating and a dimension of $0.15\times2\ \mathrm{mm}^2$. As the L-I-V curves depicted in Fig. 4(a), lasing started with a low J_{th} of 0.19 $\mathrm{kA/cm^2}$ while the operating voltage lay between 11 and 13.1 V at 15 K. The maximum optical power of ∼48 mW was obtained when the current density reached 0.38 $\mathrm{kA/cm^2}$. The maximum operating temperature of the laser is 45 K, which can be explained by the following reasons. The energy spacing of 19.2 meV between the upper level 5 and lower level 4 results in smaller kinetic energy of electrons that leads to a significant decrease in the lifetime of the upper level at elevated temperature through Fröhlich interaction, and the poor heat dissipation of the SISP waveguide structure is not conducive to high-temperature operation. A stable single-mode operation at various temperatures is presented in Fig. 4(b), where the device emitted at the frequency of 5.13 THz with an SMSR above 24 dB.

The high optical loss for the high-frequency THz DFB QCLs limits the power extraction efficiency for the devices, as shown in Fig. 5(a). The power stays almost the same for the DFB devices with and without HR coatings. This indicates that HR coating is not an effective way to improve the power output of the DFB devices. The reason is that the high loss and strong DFB coupling reduce the portion of the power emitted from the cavity. By using graded SG DFB devices to engineer the internal field distribution along the cavity, the power extraction efficiency is greatly enhanced by about a factor of 2, as shown in Fig. 5(a). It is clear that the graded sampled grating significantly improves the THz power and outcoupling efficiency compared with the DFB QCLs with or without HR

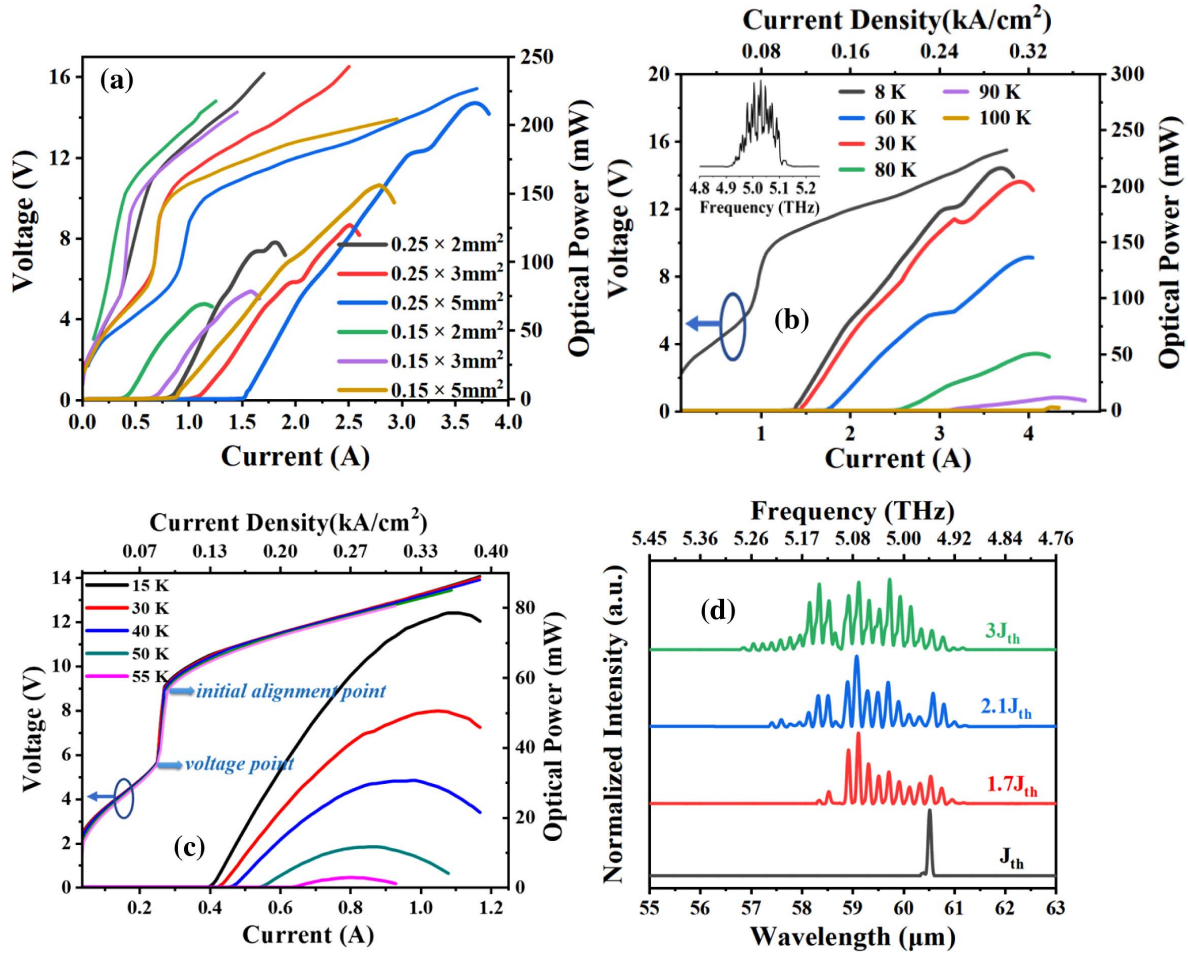

Fig. 3. (a) Light peak output power-current-voltage (L-I-V) characteristics of the FP lasers of various dimensions at 8 K. (b) Temperature-dependent L-I-V characteristics in pulsed mode of the FP laser with dimensions 0.25 × 5 mm^2. (c) Temperature-dependent L-I-V characteristics in CW mode of the FP QCL with dimensions 0.15 × 2 mm^2. (d) Emission spectra of the device shown in (c) at various injection current densities.

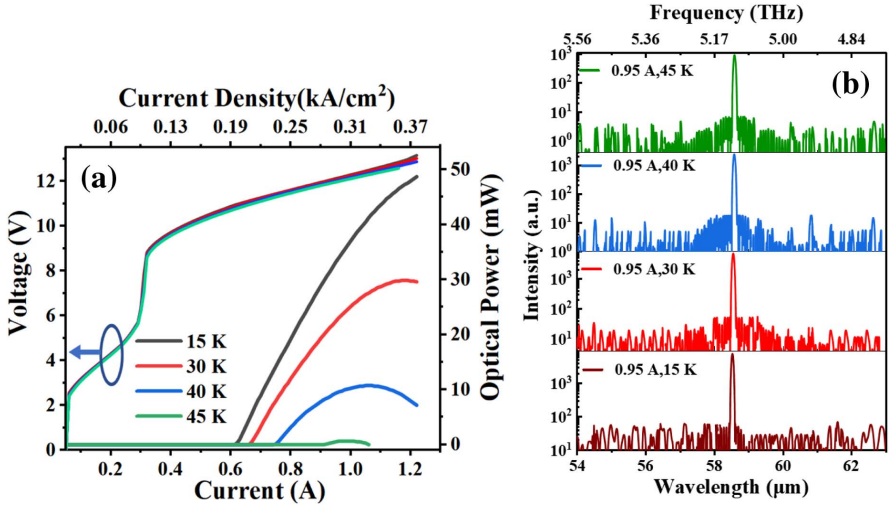

Fig. 4. (a) CW L-I-V curves of DFB QCL with the dimensions 0.15 × 2 mm^2 at various heat sink temperatures. (b) The corresponding emission spectra at various heat sink temperatures for an injection current of 0.95 A.

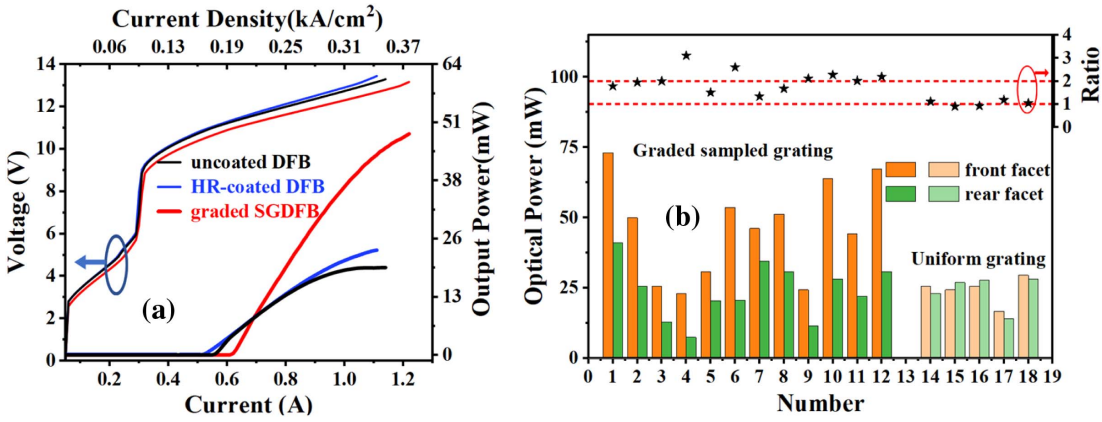

Fig. 5. (a) Output powers of coated and uncoated devices with uniform grating and device with graded sampled grating. (b) The optical powers and ratio between the front and the rear facets of 12 graded sampled DFB QCLs and five uniform grating DFB QCLs with the dimension of 0.15×2 mm^2.

coating. To further consolidate this finding, we collected and compared the optical powers of the front and rear facets of 12 DFB QCLs with graded sampled grating. The lasers operated in pulsed mode with a 1% duty cycle at a repetition frequency of 5 kHz. Figure 5(b) displays the peak optical powers and ratio between the front and the rear facets in bars and points, respectively. Although the output power of each DFB QCL varies, the power ratio between the front and rear facets is approximately 2 for all devices, indicating that the output power at the front facet of the DFB QCL is effectively enhanced via graded sampled grating, as we expected.

5. CONCLUSION

In conclusion, based on a detailed design optimization we have demonstrated the first CW operation of multimode FP THz QCLs with a maximum lasing frequency of 5.26 THz and the first single-mode CW operation of DFB QCLs emitting at the frequency of 5.13 THz. The maximum peak optical power of the FP QCLs is 220 mW at 8 K in pulsed mode, while the maximum single-mode optical power of 48 mW with an SMSR of 24 dB is obtained from the graded sampled DFB QCLs in CW mode at 15 K. The graded sampled DFB grating also exhibits an improved power outcoupling efficiency by a factor of 2 from the front facet compared with the uniform grating device. By further design and optimization of the active region, it is feasible to achieve single-mode THz QCLs at even higher frequencies with engineered field distribution using the graded sampled grating design.

Funding. National Natural Science Foundation of China (61734006, 61835011, 61991403); Key Program of the Chinese Academy of Sciences (XDB43000000, QYZDJ-SSW-JSC027); Youth Innovation Promotion Association of the Chinese Academy of Sciences (2021107).

Acknowledgment. We would like to thank Ping Liang and Fengmin Cheng for their help in the device processing.

Disclosures. The authors declare no conflicts of interest related to this paper.

Data Availability. Data underlying the results presented in this paper are not publicly available at this time but may be obtained from the authors upon reasonable request.

REFERENCES

1. M. Tonouchi, "Cutting-edge terahertz technology," Nat. Photonics **1**, 97–105 (2007).
2. S. Kumar, "Recent progress in terahertz quantum cascade lasers," IEEE J. Sel. Top. Quantum Electron. **17**, 38–47 (2011).
3. D. M. Mittleman, "Twenty years of terahertz imaging [invited]," Opt. Express **26**, 9417–9431 (2018).
4. P. Tewari, Z. D. Taylor, D. Bennett, R. S. Singh, M. O. Culjat, C. P. Kealey, J. P. Hubschman, S. White, A. Cochran, E. R. Brown, and W. S. Grundfest, "Terahertz imaging of biological tissues," Stud. Health Technol. Inf. **163**, 653–657 (2011).
5. J. F. Federici, B. Schulkin, F. Huang, D. Gary, R. Barat, F. Oliveira, and D. Zimdars, "THz imaging and sensing for security applications—explosives, weapons and drugs," Semicond. Sci. Technol. **20**, S266–S280 (2005).
6. R. Köhler, A. Tredicucci, F. Beltram, H. E. Beere, E. H. Linfifield, A. G. Davies, D. A. Ritchie, R. C. Iotti, and F. Rossi, "Terahertz semiconductor-heterostructure laser," Nature **417**, 156–159 (2002).
7. T. Fei, S. Q. Zhai, J. C. Zhang, N. Zhuo, J. Q. Liu, L. J. Wang, S. M. Liu, Z. W. Jia, K. Li, Y. Q. Sun, K. Guo, F. Q. Liu, and Z. G. Wang, "High power λ–8.5 μm quantum cascade laser grown by MOCVD operating continuous-wave up to 408 K," J. Semicond. **42**, 112301 (2021).
8. L. H. Li, L. Chen, J. R. Freeman, M. Salih, P. Dean, A. G. Davies, and E. H. Linfield, "Multi-Watt high-power THz frequency quantum cascade lasers," Electron. Lett. **53**, 799–800 (2017).
9. X. M. Wang, C. Shen, T. Jiang, Z. Q. Zhan, Q. H. Deng, W. H. Li, W. D. Wu, N. Yang, W. D. Chu, and S. Q. Duan, "High-power terahertz quantum cascade lasers with ~0.23 W in continuous wave mode," AIP Adv. **6**, 075210 (2016).
10. A. Khalatpour, A. K. Paulsen, C. Deimert, Z. R. Wasilewski, and Q. Hu, "High-power portable terahertz laser systems," Nat. Photonics **15**, 16–20 (2021).
11. C. Sirtori, S. Barbieri, and R. Colombelli, "Wave engineering with THz quantum cascade lasers," Nat. Photonics **7**, 691–701 (2013).

12. L. H. Li, I. Kundu, P. Dean, E. H. Linfield, and A. G. Davies, "High-power GaAs/AlGaAs quantum cascade lasers with emission in the frequency range 4.7–5.6 THz," in *International Quantum Cascade Lasers School and Workshop* (2016).
13. K. Fukunaga, Y. Ogawa, S. Hayashi, and I. Hosako, "Terahertz spectroscopy for art conservation," EICE Electron. Express **4**, 258–263 (2007).
14. A. J. Mayur, M. Dean Sciacca, A. K. Ramdas, and S. Rodriguez, "Redetermination of the valley-orbit (chemical) splitting of the 1s ground state of group-V donors in silicon," Phys. Rev. B **48**, 10893–10898 (1993).
15. Y. Chassagneux, Q. J. Wang, S. P. Khanna, E. Strupiechonski, E. Strupiechonski, E. H. Linfield, A. G. Davies, F. Capasso, M. A. Belkin, and R. Colombelli, "Limiting factors to the temperature performance of THz quantum cascade lasers based on the resonant-phonon depopulation scheme," IEEE Trans. Terahertz Sci. Technol. **2**, 83–92 (2012).
16. T. Grange, D. Stark, G. Scalari, J. Faist, L. Persichetti, L. D. Gaspare, M. D. Seta, M. Ortolani, D. J. Paul, G. Capellini, S. Birner, and M. Virgilio, "Room temperature operation of n-type Ge/SiGe terahertz quantum cascade lasers predicted by non-equilibrium Green's functions," Appl. Phys. Lett. **114**, 111102 (2019).
17. B. Williams, "Terahertz quantum-cascade lasers," Nat. Photonics **1**, 517–525 (2007).
18. M. Wienold, B. Röben, X. Lü, G. Rozas, L. Schrottke, K. Biermann, and H. T. Grahn, "Frequency dependence of the maximum operating temperature for quantum-cascade lasers up to 5.4 THz," Appl. Phys. Lett. **107**, 202101 (2015).
19. C. W. I. Chan, Q. Hu, and J. L. Reno, "Ground state terahertz quantum cascade lasers," Appl. Phys. Lett. **101**, 151108 (2012).
20. M. I. Amanti, G. Scalari, R. Terazzi, M. Fischer, M. Beck, J. Faist, A. Rudra, P. Gallo, and E. Kapon, "Bound-to-continuum terahertz quantum cascade laser with a single-quantum-well phonon extraction/injection stage," New J. Phys. **11**, 125022 (2009).
21. C. Sirtori, F. Capasso, J. Faist, A. L. Hutchinson, D. L. Sivco, and A. Y. Cho, "Resonant tunneling in quantum cascade lasers," IEEE J. Quantum Electron. **34**, 1722–1729 (1998).
22. K. Ohtani, D. Turčinková, C. Bonzon, I. Benea-Chelmus, M. Beck, J. Faist, M. Justen, U. U. Graf, M. Mertens, and J. Stutzki, "High performance 4.7 THz GaAs quantum cascade lasers based on four quantum wells," New J. Phys. **18**, 123004 (2016).
23. L. Mahler, R. Köhler, A. Tredicucci, F. Beltram, H. E. Beere, E. H. Linfield, D. A. Ritchie, and A. G. Davies, "Single-mode operation of terahertz quantum cascade lasers with distributed feedback resonators," Appl. Phys. Lett. **84**, 5446–5448 (2004).
24. F. Y. Zhao, Y. Y. Li, J. Q. Liu, F. Q. Liu, J. C. Zhang, S. Q. Zhai, N. Zhuo, L. J. Wang, S. M. Liu, and Z. G. Wang, "Sampled grating terahertz quantum cascade lasers," Appl. Phys. Lett. **114**, 141105 (2019).
25. H. Kogelnik and C. V. Shank, "Coupled-wave theory of distributed feedback lasers," J. Appl. Phys. **43**, 2327–2335 (1972).
26. X. F. Jia, L. J. Wang, N. Zhuo, Y. J. Guan, S. Z. Niu, J. C. Zhang, S. Q. Zhai, J. Q. Liu, S. M. Liu, F. Q. Liu, and Z. G. Wang, "Design and fabrication of a quantum cascade laser with a chirped sampling grating," OSA Contin. **2**, 1783–1790 (2019).
27. Y. J. Guan, X. F. Jia, S. S. Li, L. J. Wang, N. Zhuo, J. C. Zhang, S. Q. Zhai, J. Q. Liu, S. M. Liu, F. Q. Liu, and Z. G. Wang, "High power tapered sampling grating distributed feedback quantum cascade lasers," IEEE Photonics Technol. Lett. **32**, 305–308 (2020).